Acta Astronautica 119 (2016) 22–33

Contents lists available at ScienceDirect

Acta Astronautica

journal homepage: www.elsevier.com/locate/actaastro

Electrostatic spacecraft rate and attitude control—Experimental results and performance considerations

Daan Stevenson*, Hanspeter Schaub

Department of Aerospace Engineering Sciences, University of Colorado, Boulder, CO 80309-0431, USA

ARTICLE INFO

Article history:
Received 19 May 2015
Received in revised form
20 October 2015
Accepted 30 October 2015
Available online 7 November 2015

Keywords:
Spacecraft charging
Spacecraft attitude control
High voltage experimentation

ABSTRACT

In order to ameliorate the ever increasing space situational awareness risks at Geosynchronous (GEO) orbits, spacecraft rendezvous is desirable for servicing or repositioning operations. When large GEO spacecraft loose station keeping control, they can acquire sizable rotational momenta that imperil proximity operations and docking. Remote electrostatic charge control has been identified as a technology that may be used to safely de-spin non-spherical objects over a period of time. This paper investigates experimental pointing control results, demonstrating how the touchless electrostatic actuation can be used to arrest a tumble and control the heading in a one-dimensional setting. Further, the sensitivity of a representative system's de-spin time, required thrust profiles, and system displacement to variations in spacecraft sizes, shapes, and separation distance is considered. While the de-spin time can be reduced by allowing the servicer to vary positions, this comes at a large increase in the relative station keeping fuel costs. Using a non-spherical servicer configuration, rotating to maximize the electrostatic torque, is also shown to reduce the de-spin time by about 25%, but without significantly increasing the fuel requirements.

1. Introduction

The use of electrostatic actuation for spacecraft relative motion control has received extensive attention in the literature over the past decades [1–3]. In the Geosynchronous Orbit (GEO) environment, the favorable space plasma conditions allow for relatively low current emission to maintain non-equilibrium potentials on space objects, yielding power requirements on the order of Watts [4]. Due to the minimal mass emission of charge control devices, Coulomb actuation is essentially propellant-less and plume impingement issues associated with the use of conventional thrusters in close proximity spacecraft formations are avoided. If a spacecraft can impart relative potentials on itself and an inactive craft using a focused charged beam, touchless electrostatic maneuvers may be achieved within non-cooperative formations [5,6]. This technology is applicable to various mission scenarios intended to ameliorate the expanding orbital debris situation at GEO [7–10]. For example, an attractive electrostatic force can act as a virtual tether between the two crafts, while a low thrust maneuver is used to tow the non-cooperative object into a new orbit [11,12].

While this approach can be used to increase the semi-major axis of a GEO debris object by 300 km in two months, a docked Hohmann transfer would accomplish this in just over 12 h. Rendezvous with debris objects is complicated by the fact that uncontrolled GEO satellites may exhibit rotation rates up to 10 deg/s [13]. Meanwhile, pose algorithms and attitude matching maneuvers for rendezvous are generally restricted to rotation rates below 1 deg/s, [14,15] thus limiting the viable targets for a

* Corresponding author.
E-mail addresses: daan.stevenson@colorado.edu (D. Stevenson), hanspeter.schaub@colorado.edu (H. Schaub).
URL: http://hanspeterschaub.info (H. Schaub).

http://dx.doi.org/10.1016/j.actaastro.2015.10.023
0094-5765/

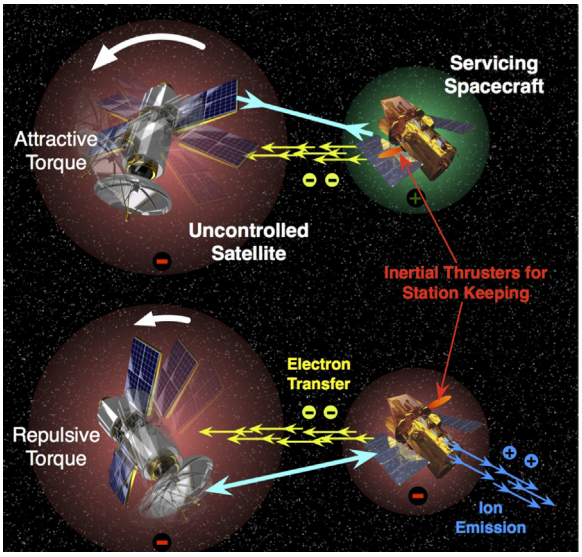

Fig. 1. Electrostatic actuation technology enabling diverse service mission profiles.

physical docking strategy. Because non-cooperative spacecraft at GEO often exhibit large moments of inertia and angular momenta, a touchless method for reducing the rotation rate prior to rendezvous is desired. Investigation of the charged Coulomb interaction between non-spherical bodies suggests that prolate bodies can experience torques and off-axis forces [16]. If these torques can be harnessed to remotely decrease the rotation of the target as depicted in Fig. 1, the trade space of candidate spacecraft for rendezvous and docking operations is greatly increased. An alternative to repositioning derelict satellites into a graveyard orbit is to service them by replenishing fuel reserves or repairing failed components. Such missions, as investigated by NASA's Satellite Servicing Capability Office and DARPA's Phoenix program, preclude the unnecessary insertion of replacement satellites.

The touchless electrostatic de-spin concept requires the servicing craft to actively control its own electrostatic potential through the use of an electron and/or ion gun. If the charged emission is aimed at the target object, the potentials of both craft can be controlled [17]. The goal is to attract the tumbling target's closest receding feature and repel its closest approaching feature, thereby de-spinning the spacecraft over time. Other work, such as Ref. [18], considers analytical dynamics and control aspects of the 3D control problem where the servicer is held at a fixed relative distance and is spherical in shape. In this earlier work, the goal of the touchless actuation is to arrest any tumbling motion. The scope of this paper considers one-dimensional rotational motion to investigate fundamental de-spin performance characteristics such as being able to control the heading in addition to the rates, as well as how to improve the de-spin time by varying a range of spacecraft servicer parameters. The one-dimensional rotation is a good assumption for many GEO debris objects, which rotate in a near-minimum energy state flat spin due to decades of internal energy dissipation. As in earlier work, the non-spherical, tumbling space body is assumed to be cylindrical, which is representative of many upper stage rocket bodies such as the Centaur as well as the once popular dual spinner satellites.

In order to develop robust charge control algorithms and create 6-DOF simulations of the Coulomb de-spin system, faster than real time determination of the electrostatic interaction between the spacecraft is necessary. Finite element approaches are too computationally expensive to achieve this, while simplified point and sphere models fail to capture torques and off-axis forces. The Multi-Sphere Method (MSM) [19,20] can model a charged spacecraft geometry using a collection of conducting spheres. Computation is limited to inverting an $n \times n$ matrix (where n is the number of spheres in the system) to obtain the charge on each sphere, followed by a summation of Coulomb's law for each sphere to determine the resulting forces and torques. The spheres can be populated throughout a given volume, or more densely spaced along the surface of a geometry, which results in a trade off between accuracy and computational costs. Previous studies utilize this electrostatic model to identify the cylinder–sphere system's equilibrium orientations and focus on Lyapunov stable nonlinear control strategies to arrest the rotation of the uncontrolled body [21,22]. These strategies have been verified with numerical simulations, while simple rate control algorithms have been tested on a rotational Coulomb charge control testbed [23].

In this paper, the touchless electrostatic performance is improved in two manners relative to earlier work. First, the new electrostatic testbed is described and its disturbance torques are characterized. New Lyapunov stable control laws are developed to arrest the one-dimensional tumble rate and control the final heading of the cylinder. The addition of heading control raises new challenges on how to prove analytical stability of this system. These control laws are experimentally demonstrated on a new electrostatic rotation testbed. Second, to optimize the design of future mission scenarios, knowledge of the impact of various system parameters on de-spin performance is necessary. Variations in separation distance as well as size and shape-scaling of the servicing spacecraft are studied to determine what effect they have on the system's de-spin time, displacement, and required stationkeeping maneuvers. Numerical simulations are used to demonstrate the expected performance change in each case.

Electrostatic detumble presents a very promising solution to the issue of rendezvous with uncontrolled space objects, but several alternatives do exist. First, the momentum transfer of the ion-sheppard method may be used to reduce rotation rates by focusing the ion beam on the appropriate half of the spinning object [24]. Lower actuation levels are achievable by this approach than the electrostatic method. Another method for touchless detumble is to use magnetic fields emitted from a chaser vehicle to impose braking eddy current torques on a foreign object. This approach would require very close proximity operations and is reliant on a fully conducting foreign object [25,26]. Lastly, laser ablation is being investigated to despin orbital debris prior to docking

operations [27]. Due to the commonality in challenges, many of these alternate technologies benefit from the theories developed in this research effort and vice versa.

2. Experimental testbed to study touchless electrostatic attitude control

2.1. Earlier experiments on electrostatic spin control

A prototype testbed allowing rotational Coulomb charge control experiments was first introduced in Ref. [23]. While this testbed demonstrated that touchless despin control experiments are feasible in a 1-G atmospheric environment, several hardware limitations were identified in this setup that restricted the performance to rotation rate control only. First, knowledge of the rotating object's angular positions was collected using a range-finding laser, which yielded noisy attitude data with insufficient accuracy. Second, active charge control was not implemented on the rotating cylinder. Rather, an initial voltage was applied to the cylinder whose gradual charge drain was characterized and modeled in the simulations. This resulted in a lack of repeatability and an inability to modulate the voltage on the cylinder during the experiment for precise control of the Coulomb torques. Lastly, the high voltage power supplies exhibited a time delay of up to one second when switching voltage polarity, thus considerably reducing the control authority in the case of large rotation rates. This earlier testbed was sufficient to demonstrate rate control. However, these limitations were an obstacle to testing and implementing a touchless heading control solution. This motivated the development of a new rotational testbed that has a faster voltage switching period and better control of the tumbling cylinder's potential, as well as improved attitude sensing capabilities.

2.2. New electrostatic testbed description

Fig. 2 depicts the improved rotational testbed for Coulomb attitude control experiments, wherein all the above limitations are addressed. The conducting cylinder is attached with a threaded interface to a rotating shaft, which is secured by the two low friction ceramic bearings. A magnetic hub is mounted to the bottom of the shaft, whose orientation is measured to within 0.35° accuracy by an absolute 10-bit analog encoder. Analysis and testing show that the magnetic fields produced by the charged rotating cylinder are sufficiently small and do not interfere with the operation of the encoder. Charge is transferred to the rotating cylinder from a Spellman CZE 2000 high voltage power supply (HVPS) via a <1 mm gap between the charging cable and a copper bushing situated on the rotating shaft. This results in ionization of the surrounding air, effectively reducing its dielectric breakdown voltage. To prevent electrical damage to the magnetic encoder in the case of an electrostatic discharge, a grounding cable is mounted underneath the encoder. The cylinder has a 15 cm diameter and a 45 cm length. The mass of the rotating components is 156.8 g, with a transverse moment of inertia of 2.867 g m^2.

The 15 cm diameter stationary sphere is located at $d=$ 45 cm from the cylinder, which results in a 15 cm surface to surface separation at a parallel orientation where the rotation angle $\theta=0^\circ$. Since the stationary sphere experiences frequent polarity changes, it is charged using the Masusada CZ9-30R power supply, which is capable of an order of magnitude quicker polarity switching than the Spellman, with verified delays lower than 0.1 s. Both power supplies are capable of supplying ± 30 kV at up to 300 μA, which results in power levels well within typical safety limits when proper precaution measures are practiced. To prevent any interaction between the operator and the charged objects, a large plastic cage surrounds the experimental setup.

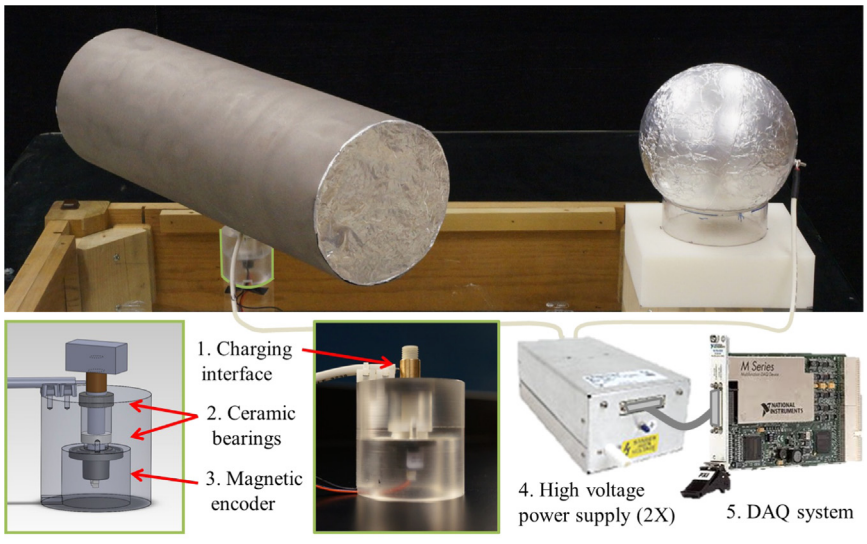

Fig. 2. Depiction of the experimental setup for charged attitude control.

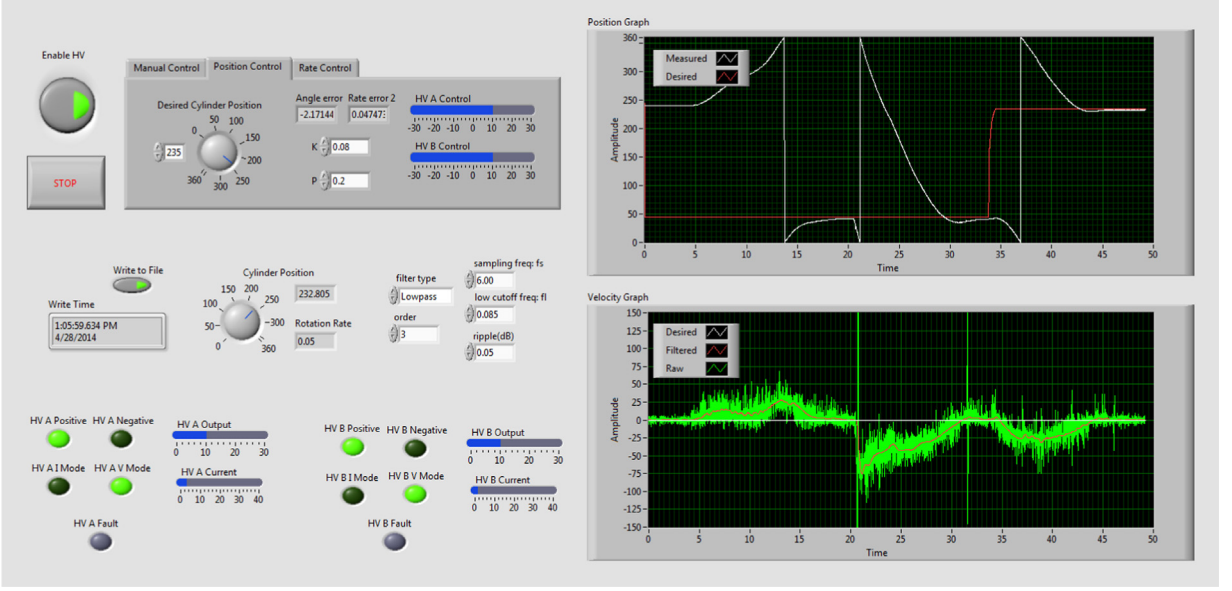

Fig. 3. Screenshot of the LabVIEW graphical user interface.

Table 1
Testbed component details.

Contactless charge transfer	HVPS cable and copper bushing
Magnetic encoder	US Digital MAE3 Absolute Encoder
Ceramic bearing	VXB.com ZrO2 $8 \times 14 \times 4$ & 688 $8 \times 16 \times 5$ full ceramic sealed bearing
High voltage power supply	Matsusada Precision CZ9-30R Spellman Voltage Electronics CZE 2000
DAQ system	National Instruments PXI-6259 data acquisition card (2X) NI SCB-68 shielded breakout boxes

Input and output controls for the power supplies and angular encoder are achieved by a PCI express based 16-Bit multi-channel NI DAQ card. National Instruments LabVIEW software is utilized to monitor and interact with the hardware. Data sampling at 66.66 Hz is achieved, which far exceeds the time constants evident in the dynamics of the system. Differentiation of the cylinder's angular position is performed within LabVIEW using a discrete derivative with switching logic to handle the multiple revolution discontinuity, which is passed through a third order lowpass Chebyshev filter. The custom graphical user interface shown in Fig. 3 allows for various operation modes, including manual voltage control, angular position control, and rotation rate control. Table 1 identifies the manufacturer and model numbers for all the hardware mentioned above.

2.3. Testbed disturbance torque characterization

As with the previous experimental setup, the two disturbance torques that act on the rotating cylinder are a constant friction torque from the ceramic bearings M_b and a rotation rate dependent atmospheric drag torque M_d. As derived in Ref. [23], these torques are given by the following expressions, where F_a is the axial force acting on the bearings from the weight of the cylinder, $\rho = 1.194$ kg/m^3 is a typical atmospheric air density, D and L are the diameter and length of the cylinder, and $\dot{\theta}$ is its rotation rate in rad/s. The remaining parameters, the bearing friction coefficient C_b and the cylinder drag coefficient C_d are to be determined empirically:

$$M_b = C_b F_a \tag{1}$$

$$M_d = \frac{\rho \dot{\theta}^2 C_d D L^4}{64} \tag{2}$$

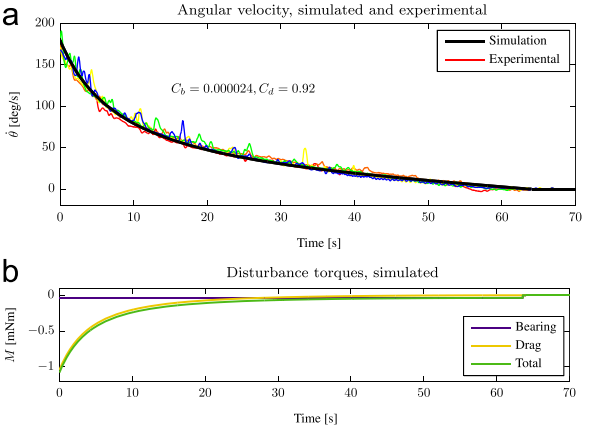

Fig. 4. Characterization of disturbance torques.

Five sets of data are collected by giving the cylinder an initial rotation and allowing it to de-spin naturally while the electric potential on both the cylinder and the adjacent sphere are held at zero. Fig. 4(a) shows the angular rates of the cylinder for each experimental run and a simulated de-spin using the modeled disturbance torques from Eqs. (1) and (2). The corresponding coefficients were tuned

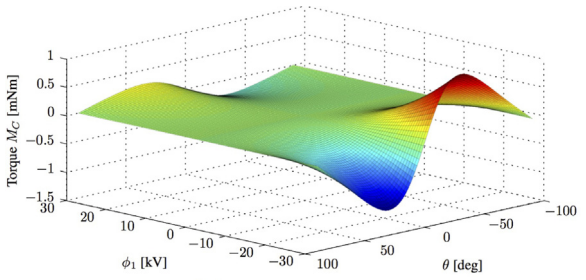

Fig. 5. Coulomb torques for various orientations and potentials of the charged rotational testbed.

until the resultant angular velocity curve optimally fit the experimental data, resulting in $C_b = 0.000024$ and $C_d = 0.92$. Fig. 4(b) shows the resulting disturbance torques in the simulation, suggesting that the drag force is dominant at angular rates higher than 33 deg/s.

3. Attitude control development and experimental verification

3.1. Analytical system dynamics

While the Multi-Sphere Method is proficient for predicting cylinder torques given the necessary orientation and voltage parameters, the nonlinear algorithms involved are not readily invertible. For control purposes, it is advantageous to determine what voltage is required to provide a desired torque at a specific cylinder orientation. Without loss of generality, it is assumed that the voltage applied to the control sphere is $\phi_1 = \phi$ and the voltage applied to the cylinder is $\phi_2 = |\phi_1|$. As a result, negative ϕ implies opposite polarity, attractive control while positive ϕ implies equal polarity, repulsive control. Fig. 5 shows the Coulomb torque M_C exerted on the cylinder for various cylinder orientations and applied potentials. This data could be used as a lookup table to determine the necessary potentials for a desired torque, but for nonlinear stability analysis, a more analytic formulation is desired.

In Ref. [21], it is assumed that the separation distance is sufficiently large for the induced charging effects to be negligible. The Coulomb torque on the cylinder is then modeled using the analytic expression

$$M_C = \gamma f(\phi) g(\theta) \tag{3}$$

where

$$f(\phi) = \phi|\phi| \tag{4}$$

and

$$g(\theta) = \sin 2\theta \tag{5}$$

From the asymmetry in Fig. 5, it is clear that the formulation above does not hold for the configuration in the experimental testbed. Due to the proximity of the shapes and the resulting induced charging effect, the torques produced by the attractive configuration are considerably larger than those imparted by electrostatic repulsion. To capture this asymmetry, a polarity dependent coefficient $\gamma(\text{sign}(\phi))$ is proposed, where γ remains always positive:

$$\gamma(\text{sign}(\phi)) = \begin{cases} \gamma_a & \text{for } \phi < 0 \\ \gamma_r & \text{for } \phi > 0 \end{cases} \tag{6}$$

Reference [18] explores alternative formulations of $g(\theta)$ to capture the non-symmetric orientation dependency at shorter separation distances. A summation of higher order terms of the form $\sin(2m\theta)$ is used, which are normalized with respect to the maximum torque angle. It was since recognized that this function is also polarity dependent, and the coefficients must change with attraction or repulsion much like γ does. Importantly, inclusion of the higher order terms does not affect the sign of $g(\theta)$, which remains positive in the first and third quadrants and negative in the second and fourth quadrants of θ. Using the polarity dependent coefficient γ and function g as described above, we obtain

$$M_C = \begin{cases} \gamma_a f(\phi) g_a(\theta) & \text{for } \phi < 0 \\ \gamma_r f(\phi) g_r(\theta) & \text{for } \phi > 0 \end{cases} \tag{7}$$

where the f function remains $f(\phi) = \phi|\phi|$ and is readily invertible to obtain the required electrostatic potentials for a desired f.

3.2. Control development

In Ref. [28], a control algorithm to drive the cylinder rate to a desired value is developed and verified on the experimental testbed. Ultimately, the novelty of this testbed is its ability to control the exact attitude of the rotating cylinder. The goal here is to track a fixed reference orientation θ_r, or minimize the error in angular position $\delta\theta = \theta - \theta_r$. The reference angle is assumed to be constant, i.e. $\dot{\theta}_r = 0$.

The involved nature of the system dynamics that result from the $g(\theta)$ function complicates the stability control arguments. To develop a heading and rate control law, the following Lyapunov function is considered:

$$V\left(\dot{\theta}, \delta\theta\right) = \frac{1}{2} I \dot{\theta}^2 + \frac{K}{2} g^2(\theta) \delta\theta^2 \tag{8}$$

This function is positive definite only within a given quadrant, as $g^2(\theta)$ vanishes at $\theta = \pi/2$. If the electric potentials are chosen such that

$$f(\phi) = -\frac{1}{\gamma}\left(g(\theta) P \dot{\theta} + g(\theta) K \delta\theta + g'(\theta) K \delta\theta^2\right) \tag{9}$$

where $g'(\theta)$ denotes differentiation with respect to θ, the resulting Lyapunov rate is

$$\dot{V}(\dot{\theta}, \delta\theta) = \dot{\theta}\left(I\ddot{\theta} + Kg(\theta)g'(\theta)\delta\theta^2 + Kg^2(\theta)\delta\theta\right) \tag{10}$$

$$\dot{V}(\dot{\theta}, \delta\theta) = -g^2(\theta) P \dot{\theta}^2 \tag{11}$$

where several terms cancel when the system dynamics

$$I\ddot{\theta} = M_C = \gamma f(\phi) g(\theta) \tag{12}$$

are included using the control in Eq. (9). This Lyapunov rate is negative semi-definite within any quadrant, implying local stability within that quadrant. The same approach can be taken as in Ref. [21] however, where the

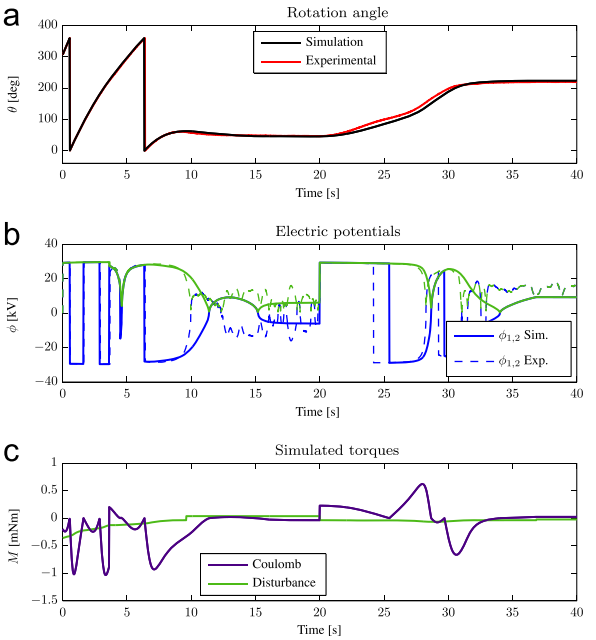

Fig. 6. Cylinder attitude control: experimental and simulation. (For interpretation of the references to color in this figure caption, the reader is referred to the web version of this paper.)

cylinder is allowed to coast without charge control until it reaches the appropriate quadrant, at which point the attitude control described above is implemented.

The control described above has been shown in simulations to converge to the desired reference attitude, but it is impractical for physical implementation because it requires exact knowledge of the higher order g function as well as its angle derivative. It is preferable to use a control based only on the sign of g, which is readily known for a given quadrant even when the polarity dependency in Eq. (7) is considered. Moreover, better time performance is provided using a control law of the following form, where K and P are chosen to be positive gains:

$$f(\phi) = -\frac{f_{\max}}{\pi/2}\text{sign}(g(\theta))\tan^{-1}\left[P\delta\dot{\theta}+K\delta\theta\right] \tag{13}$$

The arctangent function is chosen so that control voltages are smoothly limited to their maximum levels without abrupt saturation. While it is difficult to make Lyapunov stability arguments regarding this nonlinear control, we can analyze the closed loop dynamics, which take the form

$$I\ddot{\theta} = -\frac{\gamma f_{\max}}{\pi/2}\left|g(\theta)\right|\tan^{-1}\left[P\delta\dot{\theta}+K\delta\theta\right] \tag{14}$$

If we make the assumption that the reference trajectory is to maintain a constant orientation, i.e. $\dot{\theta}_r = 0$, the closed loop dynamics can be linearized about the reference angle θ_r as follows:

$$\delta\ddot{\theta}+\beta P\delta\dot{\theta}+\beta K\delta\theta = 0 \tag{15}$$

where

$$\beta = \frac{\gamma f_{\max}|g(\theta_r)|}{(\pi/2)I} \tag{16}$$

Note that both γ and $|g(\theta_r)|$ take different forms depending on whether the system is in an electrostatically attractive or repulsive state. Their signs remain unchanged however, and β is always a positive coefficient. Therefore, the roots of this second order differential equation always have negative real components, and the system is assumed to be locally stable in the linearized neighborhood of the reference angle. The natural frequency ω_n and damping coefficient ζ in this vicinity are

$$\omega_n = \sqrt{\beta K} \tag{17}$$

$$\zeta = \frac{P}{2}\sqrt{\frac{\beta}{K}} \tag{18}$$

Because β changes depending on the voltage polarities, the system will have different closed-loop response characteristics (stiffness, damping, etc.) depending on from which direction the cylinder approaches the reference orientation. Linear stability is guaranteed in either case.

3.3. Experimental results

The results in Fig. 6 demonstrate the ability to prescribe a specific angular orientation on the rotating cylinder using Coulomb actuation. The cylinder is given an initial rotation rate of 100 deg/s, at which point the charge control algorithm in (13) is implemented via the high voltage power supplies. A reference angle of $\theta_r = 45^\circ$ is prescribed while the gains are set to K=0.08 and P=0.2. Within 10 s the cylinder is brought to rest, and after a slight overshoot, the desired reference angle is achieved to within 1.5°. From Fig. 4(a) it can be seen that it takes 60 s for the cylinder to come to rest from this rotation rate by disturbance torques alone. As is evident from Fig. 6(a), the simulation conducted using MATLAB matches the experimental results with formidable accuracy. This simulation implements the full system dynamics using the three sphere MSM, including disturbance torques from bearing and atmospheric drag. Fig. 6(b) depicts the prescribed electric potentials, where blue denotes the sphere voltage ϕ_1 and green denotes the cylinder voltage ϕ_2. Here a slight deviation is evident between the simulation and experiment when the cylinder comes to rest, which is likely the result of sensor noise at low velocities.

At 20 s into the simulation, the reference angle is changed to 225°, representing a 180° switch in the desired angle. Within 12 s the target orientation is achieved, this time with a 5.5° attitude error. This is because the reference angle is approached from the direction where repulsive control is required to remove the remaining error, which produces lower torques than the attractive configuration (as seen in Fig. 5) that are unable to overcome the bearing friction. The simulation demonstrates a lower error of 2°, suggesting there is some unmodeled stiction present in the ceramic bearings. Fig. 6(c) displays the friction and Coulomb torques calculated in the simulation, which suggests a maximum Coulomb torque of roughly 1 mNm, which matches well with the results in Fig. 5.

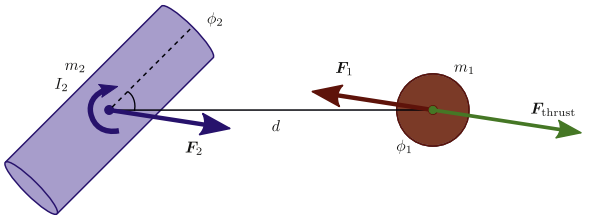

Fig. 7. Free body diagram for cylinder–sphere system.

4. Baseline de-spin and fuel usage performance

While the earlier section demonstrates how to control both rate and heading using a spherical craft with a fixed system size and location, the following work focuses on how the electrostatic torque can be increased by allowing the servicer location to move, scaling its size, or using a non-spherical rotating spacecraft. To judge the performance in each of these scenarios, a baseline performance is required as a benchmark. This is accomplished using the simplified cylinder–sphere system shown in Fig. 7, which has been used to study the remote spacecraft attitude control problem in earlier publications [21]. The angular motion of the cylinder, which might represent an upper stage rocket body such as the Centaur, is limited to 1-D rotation about its axis of maximum inertia, while the nearby spherical control craft enforces the desired electrostatic potential on the two bodies. It is assumed here that negative voltage levels up to $\phi_2 = -30$ kV are achievable on the debris cylinder, while both polarity voltage levels up to $\phi_1 = \pm 30$ kV are achievable on the circular control craft. Other bodies of work study the requirements of the charge transfer devices necessary to achieve this remote control [5,17]. The electrostatic interaction between the objects results in equal and opposite Coulomb forces $F_1 = -F_2$ on the two bodies and a control torque L_2 on the rotating cylinder.

The recently developed Multi Sphere Model (MSM) [19,20] is employed to capture the 3D electrostatic effects with a set of conductive spheres distributed throughout the geometry of the spacecraft. The MSM relies on the mutual capacitance relationship between charged spheres. Assuming a known potential is prescribed on each of the n spheres in the system, a linear system of equations can be constructed to relate the charges on the spheres to their potentials. Once this system is solved, Coulomb's law is used to determine the force on each sphere, which sum to yield the total force and torque acting on each spacecraft.

A baseline debris cylinder with a length of 3 m and diameter of 1 m is selected, with a control craft of 1 m diameter. Assuming an average density of 100 kg/m^3, this results in a 235.6 kg debris object with a 1038.43 kg m^2 transverse moment of inertia and a 52.4 kg control craft. A $d = 7$ m separation is considered, which represents a surface to surface separation of 10 craft radii when the cylinder is oriented parallel and at closest approach. It is assumed that the debris object has an initial counter-clockwise rotation rate of $\omega = \dot{\theta} = 2$ rpm $= 12$ deg/s. The charge control algorithm is simplified so that $\phi_1 = 30$ kV and $\phi_2 = -30$ kV when $0^\circ < \theta < 90^\circ$, while $\phi_1 = \phi_2 = -30$ kV when $90^\circ < \theta < 180^\circ$, ensuring constantly arresting torques.

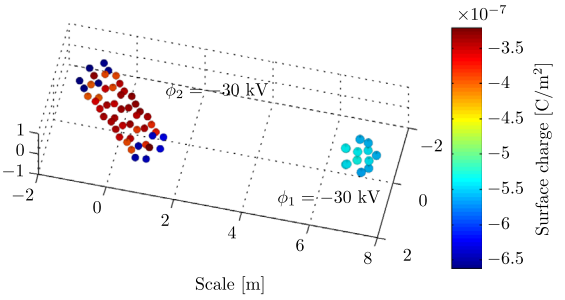

Fig. 8. SMSM for cylinder–sphere system.

Table 2
Baseline de-spin results.

Case	$F_{2,\text{ave}}$ (mN)	$L_{2,\text{ave}}$ (mNm)	Δt (h)	ΔX (km)
Single rotation average	0.219	0.150	74.43	33.37
Time dependent simulation	0.225	0.150	74.32	34.35

A thrusting force

$$\vec{F}_{\text{thrust}} = -\vec{F}_1\left(1+\frac{m_1}{m_2}\right) \tag{19}$$

is applied to the control craft in order to maintain a constant separation distance between the objects in space, resulting in a system acceleration

$$\vec{a}_{\text{sys}} = \frac{\vec{F}_2}{m_2} \tag{20}$$

When comparing the effect of various system parameters on de-spin performance, a simplified simulation is used where actuation averages are considered throughout one rotation of the debris cylinder. Since only a single rotation is considered, a higher fidelity surface Multi-Sphere Model (SMSM) as shown in Fig. 8 can be implemented [20], where 50 conducting spheres are evenly distributed along the surface of the debris cylinder and 13 spheres are used to model the control craft. As the cylinder completes one rotation, the electrostatic forces and torques are tracked. The average torque $L_{2,\text{ave}}$, which is independent of rotation rate, is used to calculate the de-spin time:

$$\Delta t = \frac{I_2 \Delta\omega}{L_{2,\text{ave}}} \tag{21}$$

Given the de-spin time, the total system displacement in deep space is calculated as

$$\Delta\vec{X} = \frac{1}{2}\vec{a}_{\text{sys,ave}}\Delta t^2 = \frac{1}{2}\left(\frac{\vec{F}_{2,\text{ave}}}{m_2}\right)\Delta t^2 \tag{22}$$

The results for the single rotation simulation are seen in the top line of Table 2. Coulomb forces and torques are quite low, but the control craft is still able to remove the 12 deg/s of rotation in just over 3 days, which is very promising for this type of operation. During that time, the entire system is displaced several dozens of kilometers,

which could be used to raise the orbit of a GEO debris satellite and benefit the eventual goal of placing the object into a disposal orbit. If the system displacement is not desired, the control craft could reposition itself to opposite sides of the rotating debris in order to achieve a net zero system displacement. Because of the induced electrostatic effects and complex capacitance relationship between charge and voltage, there is a noticeable difference in performance between the pulling and pushing configurations in different quadrants. Namely, 62.4% of the arresting torque comes from the quadrants in which the debris object and control craft have opposite polarity (pulling configuration), while only 37.6% of the effort comes from the equal polarity (pushing) configuration. The resulting difference in forces accounts for the net system displacement.

For the relative position and motion control schemes analyzed later on in the paper, a more detailed simulation is required. The de-spin operation is modeled from start to finish using an RK-45 integration, rather than extrapolating performance from a single cylinder rotation. The debris' attitude is restricted to rotation about its central axis as before, but both objects have full translational freedom. The thrust control in Eq. (19) is implemented along with a proportional derivative feedback on the desired relative position. The same baseline parameters as above are used for the initial conditions of this simulation as well as the simple quadrant dependent voltage control. In order to limit the computation time for this simulation, the three sphere MSM outlined in Ref. [19] is used to model the electrostatic interaction in the system. As is evident from Table 2, the resulting Coulomb torques and the total de-spin time agree to within a fraction of a percent with the single rotation simulation. The Coulomb force results agree to within 2.7% while system displacements deviate by about a kilometer, which results from extra errors in the discrete position feedback control algorithm. An average thrust magnitude of 1.30 mN is required to maintain the relative position in the system. If an ion thruster with $I_{SP} = 3000$ s is utilized, this results in 11.9 g of propellant expelled over the duration of the de-spin operation.

5. System parameter considerations to increase the electrostatic torque

5.1. Separation distance

It is important to understand the effect of separation distance on de-spin performance to determine what collision risks are warranted when conducting a remote electrostatic de-spin mission. Logically, the average force and torque experienced by the debris object decrease when the servicing craft is situated farther away. When varying the separation distance in the single rotation simulation discussed above, it is possible to fit the following functions with high correlation to the averaged Coulomb force and torque acting on the debris cylinder:

$$F_{2,\text{ave}} \approx 0.2136\, d^{-3.573}, \quad R^2 = 0.9974 \tag{23}$$

$$L_{2,\text{ave}} \approx 0.1076\, d^{-3.407}, \quad R^2 = 0.9985 \tag{24}$$

Since the time to remove a given rotation rate varies inversely with the average Coulomb torque, and combining Eqs. (21) and (22) yields

$$\Delta X = \frac{1}{2}\left(\frac{I_2^2 \Delta\omega^2}{m_2}\right)\left(\frac{F_{2,\text{ave}}}{L_{2,\text{ave}}^2}\right) \tag{25}$$

both the de-spin time and system displacement increase by a high power with the separation distance. As such, as close as possible a formation is desirable for the de-spin operations, while successfully mitigating collision risks.

5.2. Servicing craft size

A likely mission scenario is one where the goal is to de-spin a given satellite with specific dimensions. In this case, when designing the mission, the servicing spacecraft must be sized to optimize de-spin performance. The averaged single rotation simulation is run for various servicing craft diameters (where the baseline is a 1 m diameter), while the surface to surface separation distance is held constant at 5 m. Because the MSM spheres used to model the servicing craft spread further and further apart as the craft grows, a higher fidelity model is used with 138 spheres on the debris cylinder and 100 spheres on the control craft. As can be seen in Fig. 9, the averaged Coulomb force and torque initially grow with increasing servicing craft diameter, because the capacitance and the charge increase for a given control voltage. At larger diameters, however, the Coulomb torque drops back off because the charge that is distributed along the nonadjacent surface of the control craft becomes further and further removed from the debris cylinder. As a result, the optimal de-spin performance considering this particular cylinder occurs with a control craft diameter of 7.9 m, with diminishing returns evident at larger sizes. The system displacement is minimized at a control craft diameter of 2.6 m. Besides this tradeoff, one must consider the added structural complexity, launch cost, and charging power requirements of flying a large servicing craft.

6. Relative servicer position and orientation considerations

Besides designing the remote electrostatic de-spin mission with optimal sizing parameters as deduced from the previous section, the servicing spacecraft has the freedom to control its position and orientation in space with respect to the rotating debris object. The effects of several novel control schemes are herein analyzed. Generally, these approaches result in improvements in de-spin performance, which come at the cost of increased control forces and torques and therefore greater expenditures of fuel or power. The results, as discussed in the following sections, are compared to the baseline simulation and outlined in Table 3.

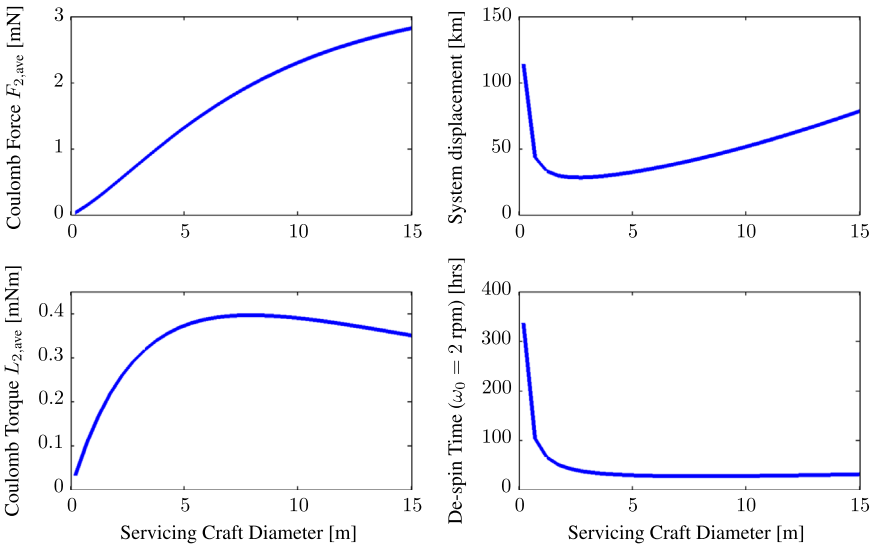

Fig. 9. Performance dependency on servicing craft size.

Table 3
De-spin control schemes results.

Case	Δt (h)	ΔX (km)	$F_{\text{thrust,ave}}$ (N)	$L_{\text{att,ave}}$ (Nm)
Baseline	74.32	34.35	0.001296	N.A.
Variable sep. distance	65.27	31.29	2.073	N.A.
Circumnavigation	37.56	N.A.	5.402	N.A.
Non-spherical servicer	56.88	29.62	0.001185	0.09974

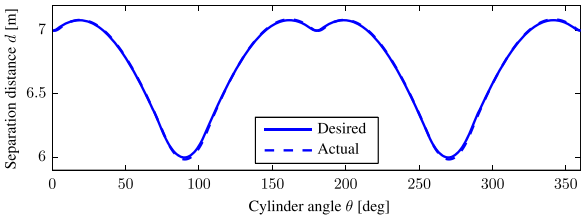

Fig. 10. Object separation for constant surface to surface distance.

6.1. Variable separation distance

In the baseline control scheme, the center to center separation distance between the two craft is held constant. In order to mitigate the collision risk that poses a threat to mission success, it is actually the surface to surface separation distance that should be maintained at a minimum distance. Therefore, a position control scheme is envisioned where the control craft moves back and forth along the straight line of separation as the cylindrical debris rotates, maintaining a constant separation from the closest surface. Fig. 10 shows the resulting desired center to center separation distance of the objects over one full rotation of the cylinder. As is evident, the control craft moves slightly further away than the baseline 7 m separation when the edge of the spinning cylinder is at closest approach.

A proportional-derivative position feedback control is implemented, utilizing the analytic derivative of the desired separation. This control maintains the relative position of the craft to within 0.021 m of the desired separation. Table 3 shows that the time to de-spin 12 deg/s of rotation decreases to 65.27 h, which represents a 12.1% increase in performance. However, the average required thrusting force increases dramatically to 2.073 N, which falls outside the range of most existing fuel-efficient propulsion technology, and would require several hundred kilograms of expended fuel using conventional bi-propellant thrusters. One can conclude that the marginal gains in performance are not worth such a large cost in fuel requirements.

6.2. Circumnavigation scheme

As the nonspherical debris object rotates, there are certain configurations for which the Coulomb control torque diminishes. Namely, when the cylinder is oriented parallel or perpendicular to the spherical servicer, no electrostatic moment is achievable. This presents the motivation for the following position control scheme, where the servicing craft circumnavigates the debris object as it rotates in order to maintain the optimal relative angle to the cylinder for maximum control torque. The same position control algorithm as before is used with larger gains to maintain a relative angle of $\theta = 42.38^\circ$, at which the cylinder experiences the maximum torque. As can be seen in Fig. 11, this scheme results in a very minute system displacement because the net Coulomb forces cancel out as the servicing craft rotates around the debris object. Because the system constantly experiences the maximum achievable torque, de-spin time is reduced by 49.5% to a mere 37.56 h. As in the previous simulation, the thrusting force necessary to maintain this relative orbit increases several orders of magnitude to 5.402 N. In this scenario, the fuel requirement might be reduced if certain natural

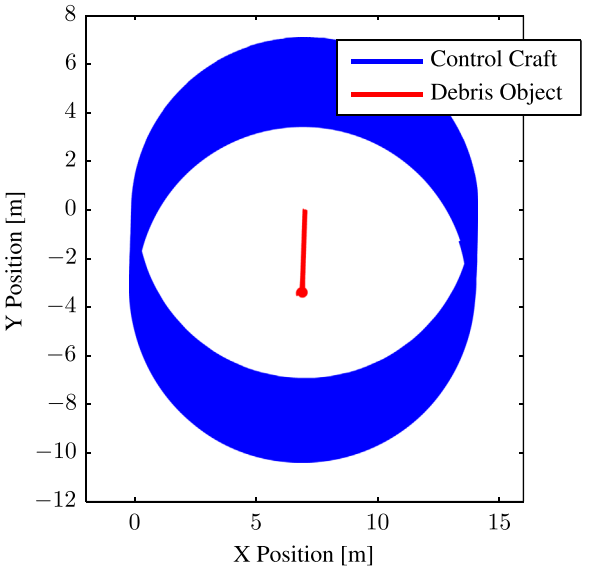

Fig. 11. Position of craft in circumnavigation scheme.

circumnavigation formation flying orbits are employed, as will be addressed during future investigations.

6.3. Non-spherical control craft

Finally, a scenario is considered wherein the control craft is no longer modeled as a conducting sphere. If de-spin gains can be achieved by adjusting the attitude of the servicer, it may be possible to improve mission performance by use of rechargeable attitude control devices rather than expending thruster fuel reserves. While a cylindrical control craft was first considered, the desired attitude profile is much more efficient using the windmill configuration depicted in Fig. 12. While the dimensions of the three sphere MSM are used, it is assumed that each of the external spheres can be charged independently. A constant relative position $d=8$ m is maintained between the spacecraft, which represents the same surface to surface separation as before. Now, however, the control craft can adjust its relative orientation to the rotating debris cylinder and specify a voltage $\phi_{1,i} = \pm$ 30 kV on any of the four external craft while the rest of the body is held at 0 kV. This will require a complex configuration of charge control devices and charge isolation surfaces.

In order to determine an appropriate control strategy, Fig. 13 shows the Coulomb torque experienced by the debris cylinder, dependent on the orientation of both objects. The control craft angle θ_1 varies between -90° and $+90^\circ$, which corresponds to one of the two closest spheres in Fig. 12 being charged. With the potential of the debris cylinder held at $\phi_2 = -30$ kV, the left plot shows the attractive torques resulting from $\phi_{1,i} = +30$ kV while the right plot shows the lesser torques that result from $\phi_{1,i} = -30$ kV. The superimposed lines show the maximum achievable counter-clockwise (red) and clockwise (blue) torque that is possible for a given debris object orientation θ_2. From this, one can deduce the desired servicing craft attitude θ_1 and which sphere should be

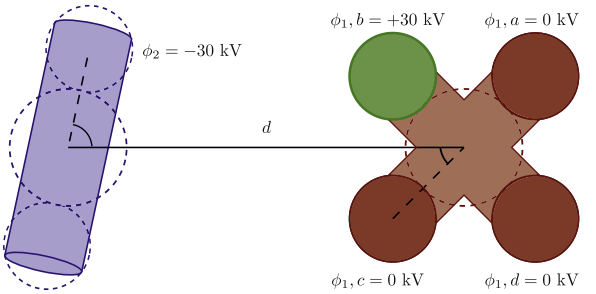

Fig. 12. Configuration for windmill control craft. (For interpretation of the references to color in this figure caption, the reader is referred to the web version of this paper.)

charged. If the cylinder in Fig. 12 with orientation $\theta_2 \approx 80^\circ$ is spinning counter-clockwise, we wish to arrest it with a clockwise torque. Accordingly, an attractive torque should be applied with $\theta_1 \approx -45^\circ$; thus an electric potential $\phi_{1,b} = +30$ kV must be applied to sphere b.

The results for the first minute of the scenario where the control craft can determine its relative orientation and which component is charged up are displayed in Fig. 14. The top plot shows what desired angle is determined from the data in Fig. 13, what angle this corresponds to for the craft once the appropriate sphere to charge is chosen, and what angle is achieved by the attitude control algorithm during the simulation. A proportional-derivative control algorithm is implemented, where the desired rotation rate is assumed to be equivalent to the debris rotation (a linearization of the curves in Fig. 13). The middle plot in Fig. 14 shows which sphere is given what voltage, and the bottom plot shows the required control moments on the servicing craft. In Table 3, it is clear that the time to remove a 12 deg/s rotation on the debris object takes only 56.88 h, a 23.5% improvement in performance. System displacement and required thrusting are reduced, while only an average of less than one tenth of a Nm control moments are required, easily achievable using conventional reaction wheels. Moreover, since the required torques are symmetric, the control moment devices will not require frequent momentum dumping. Therefore, this scenario represents a considerable performance benefit without a significant fuel cost.

7. Conclusion

This paper highlights the recent theoretical and experimental advances in remote spacecraft attitude control via Coulomb charging. Various aspects of the simplified system are analyzed, wherein a spherical control craft attempts to remove the one dimensional rotation of a cylindrical debris object. Improvements have been made on a rotational testbed, which is used to verify rate and heading control terrestrially. Such pointing control is important if a spacecraft docking maneuver is to be attempted. Besides slight deviations due to angular sensor noise, the experimental results match the numerical simulations extremely well. In order to perform a proper mission design, sensitivity of the de-spin performance to

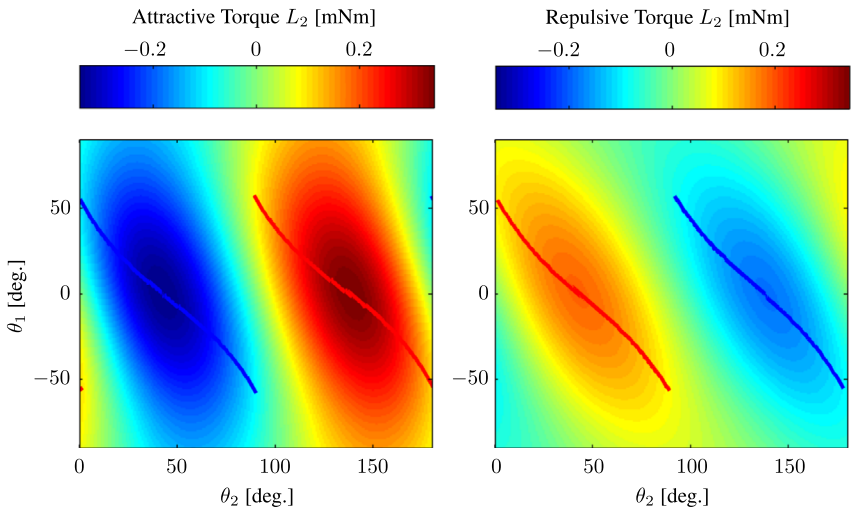

Fig. 13. Coulomb torque dependency on debris and control craft angles.

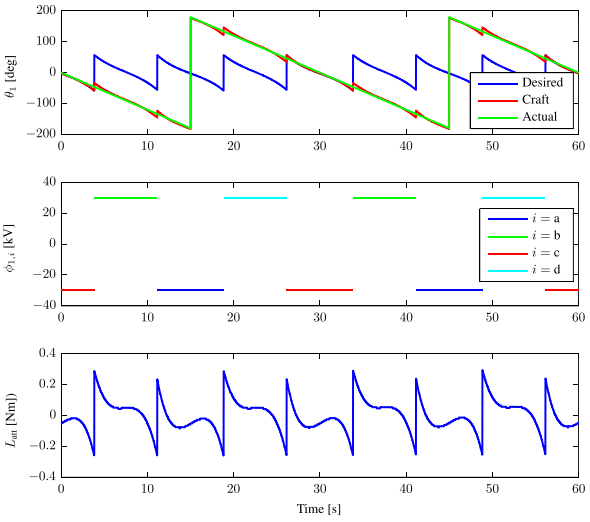

Fig. 14. Results from windmill control craft scenario.

spacecraft size, shape, and relative position is crucial. The critical result is that the closer a servicing spacecraft can get to the rotating debris, the quicker the rotation rate can be reduced. However, this objective must be carefully weighed with the collision risks associated with close proximity formation flight. Moreover, for a given debris target, increasing the size of the servicing craft will increase performance but only up to a given point, which must be balanced with the structural complexities of building large craft. Lastly, relative position profiles can improve performance and reduce de-spin times, but come at a cost of much greater control requirements.

Acknowledgments

This material is based upon work supported by the NASA Science & Technology Research Fellowship (NASA) Grant NNX11AN47H.

References

[1] J.H. Cover, W. Knauer, H.A. Maurer, Lightweight reflecting structures utilizing electrostatic inflation, US Patent 3,546,706, October 1966.
[2] L.B. King, G.G. Parker, S. Deshmukh, J.-H. Chong, Spacecraft formation-flying using inter-vehicle Coulomb forces, Technical Report, NASA/NIAC, January 2002.
[3] H. Schaub, G.G. Parker, L.B. King, Challenges and prospect of Coulomb formations, J. Astronaut. Sci. 52 (1–2) (2004) 169–193.
[4] L.A. Stiles, C.R. Seubert, H. Schaub, Effective Coulomb force modeling in a space environment, in: AAS Spaceflight Mechanics Meeting, Charleston, South Carolina, 2012, Paper AAS 12.
[5] H. Schaub, Z. Sternovsky, Active space debris charging for contactless electrostatic disposal maneuvers, Adv. Sp. Res. 43 (1) (2014) 110–118, http://dx.doi.org/10.1016/j.asr.2013.10.003.
[6] E. Hogan, H. Schaub, Space weather influence on relative motion control using the touchless electrostatic tractor, in: AAS/AIAA Spaceflight Mechanics Meeting, Santa Fe, New Mexico, 2014, Paper AAS 14-425.
[7] D. Oltrogge, D. Finkleman, Consequences of debris events in geosynchronous orbit, in: AIAA/AAS Astrodynamics Specialist Conference, Honolulu, Hawaii, 2008, Paper AIAA 2008-27375.
[8] P.V. Anderson, H. Schaub, Local debris congestion in the geosynchronous environment with population augmentation, Acta Astronaut. 94 (2) (2014) 619–628, http://dx.doi.org/10.1016/j.actaastro.2013.08.02.
[9] F. Hoots, B. Hansen, Cobra: a covariance-based debris risk assessment model, in: AAS/AIAA Astrodynamics Specialists Conference, Hilton Head, SC, 2013, Paper No. AAS 13-843.
[10] B. Hansen, Summarizing the general effects of breakup debris in geo, in: AAS/AIAA Astrodynamics Specialists Conference, Hilton Head, SC, 2013, Paper No. AAS 13-844.
[11] H. Schaub, D.F. Moorer, Geosynchronous large debris reorbiter: challenges and prospects, in: AAS Kyle T. Alfriend Astrodynamics Symposium, Monterey, CA, 2010, Paper No. AAS 10-311.
[12] E. Hogan, H. Schaub, Relative motion control for two-spacecraft electrostatic orbit corrections, in: AAS/AIAA Spaceflight Mechanics Meeting, Girdwood, Alaska, 2011, Paper AAS 11-466.
[13] P. Papushev, Y. Karavaev, M. Mishina, Investigations of the evolution of optical characteristics and dynamics of proper rotation of uncontrolled geostationary artificial satellites, Adv. Sp. Res. 43 (9) (2009) 1416–1422, http://dx.doi.org/10.1016/j.asr.2009.02.007.
[14] R. Rembala, F. Teti, P. Couzin, Operations concept for the robotic capture of large orbital debris, in: 35th Annual AAS Guidance & Control Conference, AAS, Breckenridge, Colorado, 2012, Paper No. AAS 12-018.
[15] P. Couzin, F. Teti, R. Rembala, Active removal of large debris: rendezvous and robotic capture issues, in: 2nd European Workshop on Active Debris Removal, Paris, France, 2012, Paper 7.5.
[16] L.E.Z. Jasper, H. Schaub, Effective sphere modeling for electrostatic forces on a three-dimensional spacecraft shape, in: AAS/AIAA

Spaceflight Mechanics Meeting, Girdwood, Alaska, 2011, Paper AAS 11-465.
[17] E.A. Hogan, H. Schaub, Impacts of tug and debris sizes on electrostatic tractor charging performance, in: International High Power Laser Ablation and Beamed Energy Propulsion, Santa Fe, New Mexico, 2014.
[18] T. Bennett, H. Schaub, Touchless electrostatic three-dimensional detumbling of large geo debris, in: AAS/AIAA Spaceflight Mechanics Meeting, Santa Fe, New Mexico, 2014, Paper AAS 14-378.
[19] D. Stevenson, H. Schaub, Multi-sphere method for modeling electrostatic forces and torques, Adv. Sp. Res. 51 (1) (2013) 10–20, http://dx.doi.org/10.1016/j.asr.2012.08.014.
[20] D. Stevenson, H. Schaub, Optimization of sphere population for electrostatic multi sphere model, IEEE Trans. Plasma Sci. 41 (12) (213) 3526–3535, http://dx.doi.org/10.1109/TPS.2013.2283716.
[21] H. Schaub, D. Stevenson, Prospects of relative attitude control using Coulomb actuation, in: Jer-Nan Juang Astrodynamics Symposium, College Station, TX, 2012, Paper AAS 12-607.
[22] T. Bennett, D. Stevenson, E. Hogan, L. McManus, H. Schaub, Prospects and challenges of touchless debris despinning using electrostatics, in: 3rd European Workshop on Space Debris Modeling and Remediation, CNES, Paris, 2014, Paper P8.
[23] D. Stevenson, H. Schaub, Terrestrial testbed for remote Coulomb spacecraft rotation control, Int. J. Sp. Sci. Eng. 2 (1) (2014) 96–112.
[24] C. Bombardelli, H. Urrutxua, M. Merino, E. Ahedo, J. Pelaez, J. Olympio, Dynamics of ion-beam-propelled space debris, 22nd International Symposium on Space Flight Dynamics, Sao Jose dos Campos, Brazil, 2011.
[25] N. Ortiz Gómez, S.J.I. Walker, Eddy currents applied to de-tumbling of space debris: feasibility analysis, design and optimization aspects, in: 40th COSPAR Scientific Assembly, 2–10 August 2014, Moscow, Russia, Abstract PEDAS.1-30-14, COSPAR Meeting, vol. 40, 2014.
[26] F. Sugai, S. Abiko, T. Tsujita, X. Jiang, M. Uchiyama, Detumbling an uncontrolled satellite with contactless force by using an eddy current brake, IROS' 13 (2013) 783–788.
[27] R. Kumar, R.J. Sedwick, Despinning orbital debris before docking using laser ablation, J. Spacecr. Rocket. 52 (4) (2015) 1129–1134.
[28] D. Stevenson, H. Schaub, Advances in experimental verification of remote spacecraft attitude control by Coulomb charging, in: GNC 2014: 9th International ESA Conference on Guidance, Navigation and Control Systems, Porto, Portugal, 2014.